Three-Step Spin Crossover in a Pseudo-3D Hofmann Type Complex Originating from Anisotropic Supramolecular Interactions

Xiaochun Li[a], Nour-El-Islam Belmouri[b], Mouhamadou Sy[b,c], Mariusz Wolff[d], Aurelian Rotaru[e], Steven van Terwingen[f], Dominik Maskowicz[g], Miroslaw Sawczak[g], Rafal Jendrzejewski[g], Kamel Boukheddaden[b*] and Yann Garcia[a*]

[a]Institute of Condensed Matter and Nanosciences, Molecular Chemistry, Materials and Catalysis (IMCN/MOST), Université catholique de Louvain, 1348 Louvain-la-Neuve, Belgium

[b]Université Paris-Saclay, UVSQ, CNRS, GEMAC UMR 8635, 45 Avenue des Etats Unis, F-78035 Versailles Cedex, France

[c] Université Assane Seck de Ziguinchor, Département de Physique, LCPM, BP 523 Diabir, Ziguinchor 27000, Sénégal

[d]Institute of Functional Materials and Catalysis, Faculty of Chemistry, University of Vienna, Währinger Str. 38-42, 1090 Vienna, Austria

[e]Department of Electrical Engineering and Computer Science and MANSiD Research Center, "Stefan cel Mare" University, University Street, 13, Suceava 720229, Romania

[f]Institute of Inorganic Chemistry, Faculty of Chemistry, University of Vienna, Währinger Str. 42, 1090 Vienna, Austria

[g]Photophysics Department, The Szewalski Institute of Fluid-Flow Machinery, Polish Academy of Sciences, Fiszera 14, 80-231 Gdańsk, Poland

ABSTRACT

The development of multistep spin crossover materials is of considerable interest for molecular information processing and sensing applications, and remain synthetically and mechanistically challenging. Herein, we present the first iron(II) two-dimensional Hofmann structure containing 1,2,4-triazole derivatives and $[Au(CN)_2]^-$ units, namely $Fe(MeOPhtrz)_2[Au(CN)_2]_2$ (**1**, MeOPhtrz = (*E*)-1-(2-methoxyphenyl)-*N*-(4*H*-1,2,4-triazol-4-yl)methanimine). The complex exhibits a temperature-induced three-step spin crossover behavior, confirmed by magnetic susceptibility, differential scanning calorimetry, Raman spectroscopy, single crystals X-ray diffraction (SXRD) and optical microscopy. SXRD reveals a pseudo-three-dimensional structure assembled through multiple intermolecular interactions, including hydrogen bonding, π-π stacking and π-Au interactions. These interactions contribute to an anisotropic supramolecular framework that induces a multi-step spin crossover process. The sequential spin

transition is likely driven by the differential rigidity along the crystallographic axes and the varied response of Fe-N bond lengths, leading to distinct transition steps. This study highlights the significance of supramolecular interactions in governing spin crossover properties and opens new avenues for the design of 2D Hofmann-like materials with tunable functionalities.

INTRODUCTION

Bistable molecules are considered as suitable candidates to be implemented as molecular components of electronic devices of next generation.[1,2] In particular, iron(II) spin crossover (SCO) molecules given that they can be switched between a diamagnetic, low-spin (LS) ground state (logical state 0) and a paramagnetic high-spin (HS) state (logical state 1), in response to an external stimuli, including temperature, pressure or light-irradiation.[3-6] These two states are often associated with distinct magnetic, optical, and structural properties, offering the basis for switchable molecular functionalities.

Beyond simple bistability, SCO materials that exhibit two-step or multistep transitions provide enhanced control over the switching process and enable access to intermediate or fractional spin states.[7,8] Such systems offer the prospect of multistate logic, ternary data storage, or stepwise modulation of physical responses. Two-step transitions are more common and can result from symmetry breaking,[9,10] inequivalent Fe(II) sites,[11-14] or short-range ordering effects.[15] In contrast, materials exhibiting three or more SCO steps are extremely rare, and their formation typically relies on the involvement of guest molecules, as well as the delicate interplay between structural cooperativity, lattice elasticity, and supramolecular interactions to stabilize multiple intermediate spin states.[16-18]

In particular, 2D Hofmann-type structures made of a bimetallic layered coordination polymer structure which provides a flexible platform for fine-tuning intermolecular and intramolecular interactions by adjusting interlayer spacing through synthetic modifications. These structural characteristics enabled the realization of multistep, abrupt and hysteretic spin transitions.[19-21] Numerous studies have reported two distinct types of structures: (i) with 1,2,4-triazole derivatives as ligands, connected by square planar $[M^{II}(CN)_4]^{2-}$ units (M = Pd, Pt, or Ni);[22-27] (ii) with linear $[M(CN)_2]^-$ units (M = Au or Ag) as bridging linkers, with pyridine, pyrimidine, bipyridine, or other *N*-heteroaromatic rings serving as organic ligands.[28-34] To date, there have been however no reports of 2D layered SCO Hofmann-type compounds with 1,2,4-triazole derivatives as ligands and $[M(CN)_2]^-$ (M = Au or Ag) as bridging units. Although Neville *et al.* described a Fe^{II}-1,2,4-triazole trimer linked by $[Au(CN)_2]^-$, the compound coordinated as a hybrid 1D chain rather than a 2D layered structure.[35]

In this work, we present the first example of a 2D Hofmann-type structure incorporating both a 1,2,4-triazole derivative ligand and $[Au(CN)_2]^-$ units. Remarkably, this compound exhibits a well-defined, temperature-induced three-step SCO behavior, as confirmed by crystallographically, magnetically, Raman spectroscopy, as well as by differential scanning calorimetry and optical microscopy. Our findings highlight how anisotropic supramolecular interactions contribute to the emergence of this rare multistep SCO behavior in a layered architecture.

RESULTS AND DISCUSSION

Synthesis and characterization

Light green crystals of **1** were obtained by slow evaporation at room temperature from a solution prepared by dissolving **MeOPhtrz** and $Fe(ClO_4)_2 \cdot 6H_2O$ in methanol, and $K[Au(CN)_2]$ in water. Crystals were collected by filtration and used for further characterization. Formulation of $Fe(MeOPhtrz)_2[Au(CN)_2]_2$ [**1**, **MeOPhtrz** = (*E*)-1-(2-methoxyphenyl)-*N*-(4H-1,2,4-triazol-4-yl)methanimine)] was determined by both high resolution mass spectrometry and elemental analysis. Absence of lattice or adsorbed solvent molecules in **1** was confirmed by Thermogravimetric analysis (TGA) that shows no significant mass loss below 200 °C (Figure S2). The IR spectrum of **MeOPhtrz** displays a characteristic band corresponding to C=N stretching at 1597 cm^{-1} (Figure S1). Upon coordination to Fe(II), this band undergoes a slight shift, indicating coordination of the 1,2,4-triazole nitrogen to the Fe(II) center. In addition, a strong absorption band observed at 2176 cm^{-1} confirms the presence of coordinated $[Au(CN)_2]^-$ units (Figure S1).

Scanning electron microscopy (SEM) analysis carried out for **1** at room temperature revealed well-defined block-like crystals with a distinct layered morphology and smooth surfaces (Figure S3). High-magnification images display step-like growth features indicating an ordered crystallization process. Phase purity of **1** was confirmed by powder X-ray diffraction (PXRD), with the experimental pattern at room temperature showing good agreement with the simulated pattern based on single-crystal data (Figure S4).

Crystallographic analysis. Crystallographic data were collected at different temperatures to assess the structural changes associated with spin transitions of **1**. Data collection was first run at 200 K, after which the sample was heated to 300 K, then cooled to 100 K, and finally heated again at 300 K to check the robustness of the crystal across a wide temperature range (200 K). **1** crystallizes in the monoclinic *C*2/*c* space

group at all temperatures. For the sake of simplicity, a slight disorder of the triazole moieties will not be discussed here (Figure S5). Figure 1 shows the crystal structure at 100 K and packing diagram. The central Fe(II) ion forms an electrically neutral 2D Hofmann layer with an FeN_6 topology, coordinated by two symmetrically positioned **MeOPhtrz** ligands in axial positions and four $[Au(CN)_2]^-$ ligands in equatorial positions. The structure contains one Fe site and two crystallographically independent Au sites, Au1 and Au2. The chain connected through the Au1 site is aligned at 180°, while the chain connected through the Au2 site exhibits a significant deviation from 180°. The angles between the three connected iron atoms at 100 K, 200 K and 300 K are 156.7°, 156.42° and 155.65°, respectively (Figure S6). This deviation causes the 2D layers to display an octahedral tilt relative to the ideal planar configuration, resulting in undulating layers. Crystallographic data, representative bond lengths and distortion parameters are shown in Table S1 and Table S2. At 300 K, the unit cell volume is 2914.4(3) $Å^3$ with $Z = 4$. The Fe-N bond lengths range from 2.126 to 2.199 Å with an average of 2.161 Å, which indicates HS Fe(II) ions. The distortion parameter $\sum$, which indicates the degree of deviation of the metal ion from the ideal octahedral geometry, was calculated to be 26.8°, while Θ, which represents the degree of distortion from the octahedral structure to the triangular prism structure, was calculated to be 81.75°. At 200 K, the Fe-N bond length decreases to 2.022 to 2.076 Å, with an average of 2.047 Å, suggesting the presence of LS species within the system. Upon cooling to 100 K, the distortion parameters $\sum$ and Θ are 20.5 and 72.56°, respectively. The average Fe-N bond length decreases to 1.958 Å, indicating that Fe(II) ions have fully switched to the LS state. The Hofmann layered framework structure basically remains unchanged over the entire temperature range investigated (300-100 K).

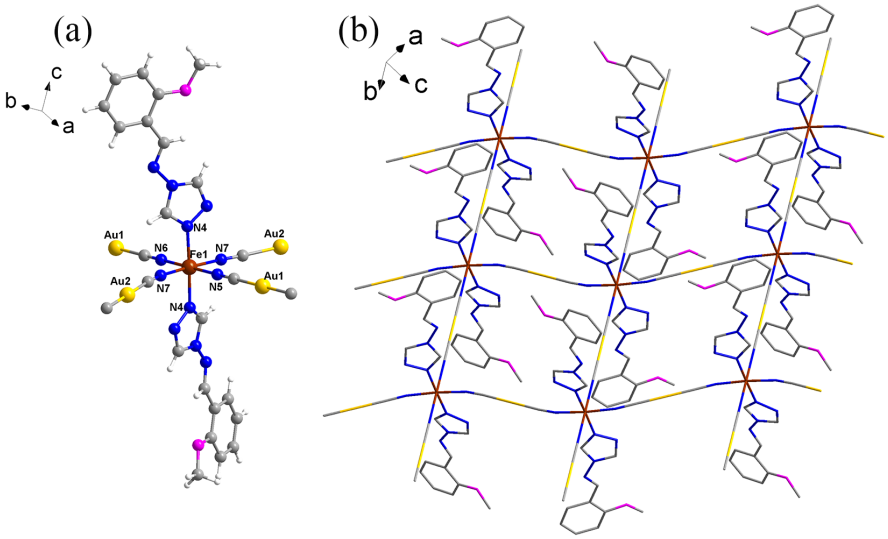

Figure 1. (a) Molecular structure of **1** at 100 K. Color code: atoms Fe in brown, O in pink, Au in yellow, N in blue, C in grey, H in white. (b) Packing diagram showing the 2D structure of **1** at 100 K. H atoms

were omitted for clarity.

A variety of intermolecular interactions are found in **1**, including hydrogen bonding, π-π stacking interactions between the triazole ring and the phenyl group, and π-Au interactions between gold atoms and benzene rings. These interactions are especially located along the *c* axis, resulting in a more rigid behavior in this direction. The cavities produced by the two-dimensional net are filled with two **MeOPhtrz** ligands from adjacent nets. As these penetrating **MeOPhtrz** ligands exhibit a conjugated π-system, it can form favorable interactions with Au2. The supramolecular packing structure and representative intermolecular contacts are shown in Figure 2 and Tables S3-S5, respectively. The strength of these interactions varies at different temperatures, affecting the spin state of the compound. Figures S7 illustrates the temperature-dependent evolution of π–π stacking and Au–π interactions. Despite the compound's intrinsically 2D nature, these intermolecular interactions drive its assembly into a pseudo-3D architecture (Figure S8). Unlike the previously reported $[Au(CN)_2]^-$ bridged Hofmann compounds, such as $Fe(quinazoline)_2[Au(CN)_2]_2$,[34] or $[Fe(Phpz)_2\{Au(CN)_2\}_2]$,[36] which both feature Au···Au interactions, the Au···Au distances in **1** of 7.073, 7.117 and 7.172 Å at 100 K, 200 K and 300 K, respectively, are too large to support aurophilic interactions. This could be attributed to the rigidity of the **MeOPhtrz** ligand, the substantial steric hindrance and π-Au interactions formed between Au atoms and benzene rings. Interestingly, this additional steric hindrance as well as intermolecular interactions also make **1** different from the reported complexes $[Fe_3(bztrz)_8(Au(CN)_2)_4]\cdot 2\{Au(CN)_2\}\cdot$guest (where ***bztrz*** is (*E*)-1-phenyl-N-(1,2,4-triazol-4-yl)-methanimine), which consists of a trimer of Fe(II) sites coordinated by six ***bztrz*** ligands and another outer Fe(II) site bridged by four ***bztrz*** ligands and two $[Au(CN)_2]^-$ anions, forming a 1D chain.[35]

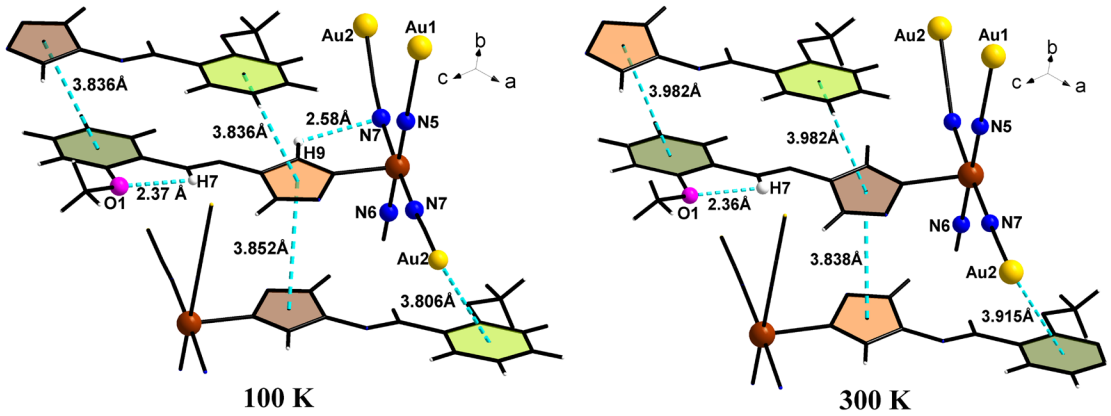

Figure 2. Supramolecular interactions in **1** at 100 K (left) and 300 K (right), highlighting temperature-dependent changes in intermolecular contacts. Cyan dashed lines represent hydrogen bonding, π···π stacking, and Au···π interactions. While hydrogen bond distances (e.g., O1···H7) remain largely unchanged with temperature, π···π and Au···π contacts exhibit noticeable elongation (from 3.836 Å to

3.982 Å and from 3.806 Å to 3.915 Å, respectively), indicating their structural flexibility and potential role in the multi-step spin transition behavior. Atom colors: Fe (brown), Au (yellow), N (blue), O (pink), C (grey), H (white).

Magnetic Properties. Variable-temperature magnetic susceptibility measurements were conducted over the range 4-300 K under both cooling and warming modes for **1** (Figure 3) where χ_M represents the molar magnetic susceptibility and T the temperature. A gradual spin-state transition was recorded between 255 K and 145 K. The $\chi_M T$ value remains constant at 3.21 cm^3 K mol^{-1} between 300 K and 255 K, which is within the expected range for HS Fe(II) ions. As the temperature decreases, the $\chi_M T$ value gradually drops to approximately 1.35 cm^3 K mol^{-1} around 195 K, with a slight change in the transition rate observed. A pseudo-plateau is evident between 190 K and 187 K. At 186 K, the $\chi_M T$ value declines slightly more sharply. When the temperature reaches 145 K, the $\chi_M T$ value decreases to 0.23 cm^3 K mol^{-1}, indicating a practically complete transition to the LS state. The curves from the second and third set of measurements completely overlap, demonstrating a reversible transition (Figure S9). Most interestingly, the derivative $d\chi_M T/dT$ reveals a spin transition proceeding in three steps, with transition temperatures $T_1^{\uparrow}$ = 185 K, $T_2^{\uparrow}$ = 192 K and $T_3^{\uparrow}$ = 231 K (Figure 3, inset). On cooling, a narrow hysteresis loop is identified at $T_1^{\downarrow}$ = 183 K. A narrow plateau was also observed for SCO Hofmann-type compounds bridged by $[M(CN)_2]^-$ (M = Au, Ag) displaying stepwise transitions.[34,37-41] Such a plateau is likely attributable to interactions within the complex 2D layered structure,[34] which influence the cooperativity of the SCO process, resulting in a transition proceeding in multiple discrete steps rather than as a single and continuous process.

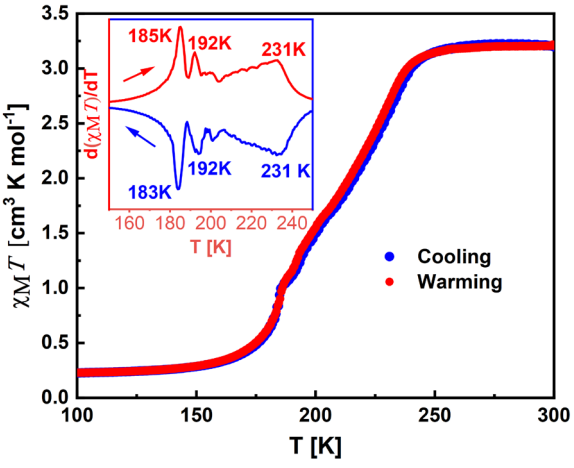

Figure 3. Temperature dependence of $\chi_M T$ for **1** over the range 100-300 K. The inset displays the first derivative of $\chi_M T(T)$ in warming and cooling modes at 2 K min^{-1}, 1000 G, evidencing clearly a three step SCO behavior.

Calorimetric Measurements. Differential scanning calorimetry (DSC) measurements were conducted under a nitrogen atmosphere with a scanning rate of 5 K min^{-1}, covering the 120 K to 298 K (Figure 4). During the cooling process, three exothermic peaks were observed at 181 K, 189 K and 229 K. The enthalpy and entropy changes during transition are calculated as ΔH = 8.3 kJ mol^{-1} and ΔS = 38.9 J K^{-1} mol^{-1}, respectively. Besides the eigenvalue of the electronic contribution to the entropy $R \cdot \ln(5)$ = 13.4 J mol^{-1} K^{-1}, the main vibrational contribution to the system entropy was evaluated to be ΔS_{vib} = 25.5 J mol^{-1} K^{-1}, within the experimental range typically observed for Fe(II) SCO complexes.[42] Similarly, three endothermic peaks were detected during the warming process, with slightly shifted peak positions at 185 K, 191 K and 230 K, resulting in the appearance of a small thermal hysteresis loop. The DSC profile is in good agreement with SQUID measurements (Figure 3), unambiguously confirming the occurrence of a three-step spin transition below the room temperature region for **1**.

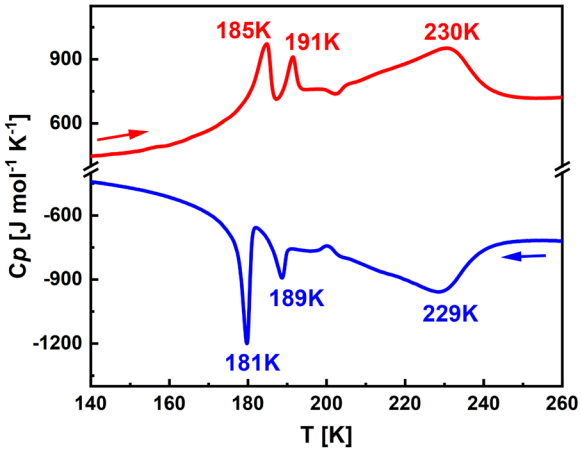

Figure 4. DSC profile for **1** in the cooling and warming modes. The signals recorded during the cooling and warming modes are shown in blue and red, respectively.

Raman Spectroscopy. Since the Fe-N bond length and molecular structure of **1** change during the SCO process, Raman spectra in the HS state (300 K) and LS state (110 K) were first collected (Figure 5a). The spectra show that the intensity of characteristic vibration bands changes significantly. The low-frequency region (0–600 cm^{-1}) primarily involves Fe-N and ligand framework vibrations, where the band at 152 cm^{-1} is likely attributed to lattice vibrations, associated with the overall movement of Fe(II) and its coordinating ligands.[43] During the HS to LS transition, the Fe-N bond lengths shorten, thereby restricting the extent of lattice vibrations and resulting in a significant decrease in the intensity of the corresponding Raman bands. The 339 cm^{-1} peak is attributed to Fe-N bending vibrations, which are more active and more easily excited in the HS state, resulting in a stronger Raman signal. In contrast, the 556 cm^{-1} peak corresponds to Fe-N stretching vibrations and appears more intense in the LS state,

indicating Fe-N bond shortening and increased rigidity in the LS state. The mid-frequency region (600-1600 cm^{-1}) mainly involves C=N stretching vibrations and 1,2,4-triazole ring deformation modes,[44] while the high-frequency region (>2000 cm^{-1}) is dominated by Au-CN stretching vibrations, characteristic of metal-cyanide complexes.[45]

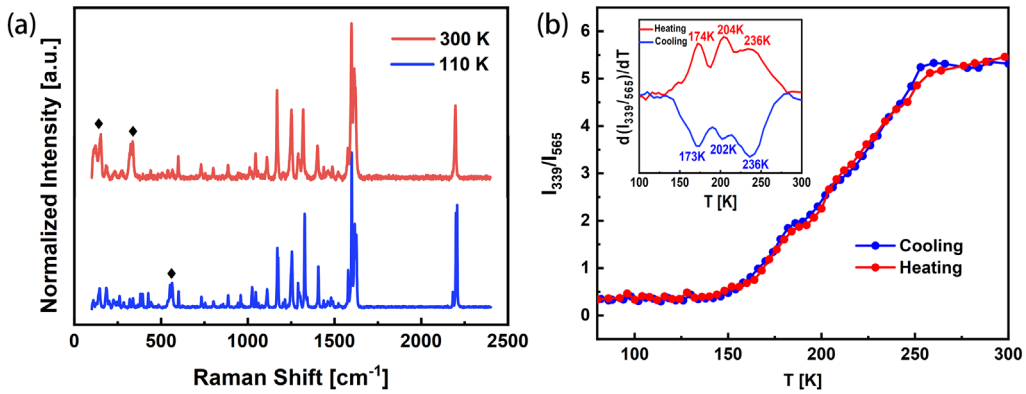

Figure 5. (a) Selected Raman spectra of **1** collected at 300 K (HS state, red) and 110 K (LS state, blue). The diamond symbols (◆) highlight key spin-state sensitive peaks, located at 152, 339, and 556 cm^{-1}, which are discussed in the text and attributed to Fe–N lattice, bending, and stretching vibrations, respectively. (b) Temperature dependence of the intensity ratio of the 339 and 556 cm^{-1} Raman bands (I_{339}/I_{556}) recorded at 1 K min^{-1}. The inset shows the first derivative *vs*. temperature.

Raman spectra were recorded over a wide range of temperatures (77-350 K) at a scan rate of 1K/min to cover the SCO range. The temperature dependence of the intensity ratio of two characteristic bands (I_{339}/I_{556}) was plotted as a function of temperature (Figure 5b). The ratio remains nearly constant on cooling between 300 and 260 K, after which it gradually decreases, with a slight change in slope observed between ca. 200 and 192 K. A relatively smooth step occurs between 192 and 184 K, followed by a faster decrease until ca. 150 K, where the ratio levels off, indicating that the compound has almost fully converted to the LS state. The heating and cooling curves are essentially similar, confirming the reversibility of the transition. The first derivative analysis further reveals the multistep nature of the transition, with transition temperatures determined at 173, 202 and 236 K on cooling, and at 174, 204 and 236 K on warming. These transition temperatures are slightly shifted compared to magnetic (Figure 3) and calorimetric (Figure 4) data, presumably due to local laser-induced heating, as reported for related SCO systems.[37]

Cryogenic optical microscopy. Cryogenic optical microscopy (OM) studies[46-52] of selected single crystals of **1** (Figure S10) were performed over the temperature range 130-270 K, to monitor the colorimetric changes of the spin transition. High-quality

single crystals of size between 408 µm and 231 µm in length and 107 µm and 149 µm in width were selected for the present OM investigations (see movie S1, available as a separate file in the Supporting Information). Figure 6 shows selected snapshots of a single crystal undergoing a thermally induced phase transition with a homogeneous transformation, related to cooling and heating processes, where the LS and the HS states correspond to red and light areas, respectively, of the crystal. The associated real-time dynamics of this spin transition are provided in movies S2 and S3 for the cooling and heating processes, respectively. These results indicate that, at the start of the HS to LS transformation on cooling, the crystal undergoes a first gradual transformation at 230 K, while from 200 K, we identify another color change where the crystal becomes darker red at the end, followed by the appearance of some domains in volume. A similar behavior is also obtained on warming.

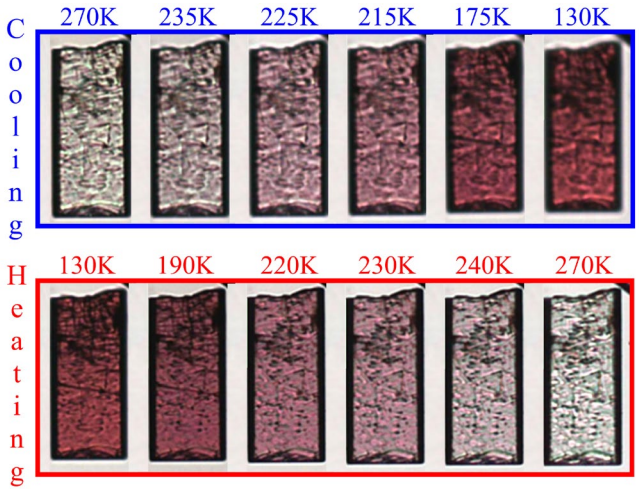

Figure 6. Selected snapshots showing the homogeneous behavior of the crystal of **1** ($L \times \ell \approx 231\ \mu m \times 107\ \mu m$) during the spin transition along cooling and heating branches of the thermal hysteresis recorded at a scan rate of 2 K min^{-1}.

The detailed inspection of the OM data shows that during cooling, the crystal changes from colorless transparent to pink or light red at the level of the first step of the OD curve of Figure S10 through a homogeneous transformation. This behavior is better identified in the raw movies S4 (cooling) and S5 (heating) in which we correlated the real-time evolution of the OD with the spatiotemporal changes.

As for the domains accompanying the spin change, they are hardly visible in Movies S1 and S2 due to the compression of the video (which lasts 1h 10min) so that it plays in 21s. This technical point is discussed in great details in the SI where we provide long version videos (movies S6 and S7), showing the appearance of domains at the transition.

Given the high sensitivity of the camera to the green channel, the green optical density (OD) was analyzed to determine the HS fraction. We have monitored the spatiotemporal evolution of the spatially averaged green OD, which was evaluated in each pixel, using

a specific Matlab program, developed for the image processing of OM movies (Movies S2 and S3, provided as separate files in the Supporting Information). Figure 7 displays the thermal dependence of the HS fraction, showing the existence of a thermal hysteresis with three multistep transitions located between 240-232K, 194-184K and 186-176K with the occurrence of slight plateaus along the switching branches. The corresponding transition temperatures were determined after deriving the HS fraction and plotting the thermal dependence of its derivative with temperature, as shown in insert for a scan rate of 2 K min^{-1}. The obtained behaviors are compared to those of magnetic measurements (Figure 3, S11 and S12). Moreover, an increase in the scan rate to 4 K min^{-1} (Figure 7) is in line with those reported on different SCO compounds. [52,53]

From a theoretical point of view, the dependence of the transition temperature on the scan rates is due to the appearance of metastable states just below the transition. The lifetime of these metastable states (LS on heating, and HS on cooling) is finite, and playing with temperature sweeping rate allows interfering with their relaxation.[54]

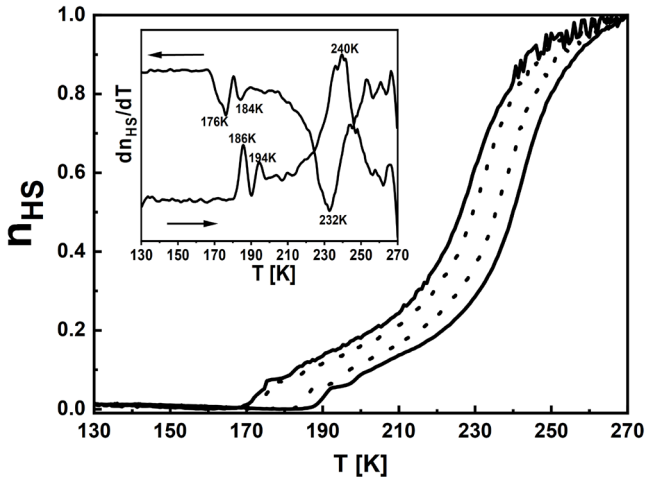

Figure 7. Thermal dependence of the HS fraction, n_{HS}, derived from the spatially averaged OD, showing the presence of hysteretic multistep spin transitions for two temperature kinetics: 4 K min^{-1} (full line) and 2 K min^{-1} (dashed line). The insert shows the thermal dependence of the derivatives dn_{HS}/dT of the cooling and heating branches at 2 K min^{-1}. Data were smoothed before calculating dn_{HS}/dT, to avoid the presence of singularities, due to the observed fluctuations.

A soft variation of n_{HS} between 170 and 200 K was noticed. Derivative analysis (dn_{HS}/dT) reveals however several distinct inflection points in this range. These features indicate subtle but detectable variations in the HS population, which may reflect partial or domain-limited spin transitions involving a small number of Fe(II) sites. This interpretation is further supported by complementary magnetic susceptibility (Figure 3) and DSC measurements (Figure 4). The variation in optical microscopy is weaker because the investigations are carried out on only one single crystal, whereas magnetic and calorimetric measurements involve an assembly of crystals. Nevertheless,

the first derivative analysis (Insert to Figure 7), which is more sensible, clearly reveals these features, along with the corresponding transition temperatures.

Thermal evolution and anisotropic deformation of lattice parameters

To gain deeper insight into the structural behavior of **1** under varying thermal conditions, single-crystal X-ray diffraction measurements were conducted across the temperature range 175 K - 245 K on both cooling and warming modes. Data for relevant lattice parameters of the *C*2/*c* space group and unit cell volume *V*, were collected at 5 K intervals in both heating and cooling modes at a constant temperature (Figure 8 and Table S6). As the temperature increases, all evaluated parameters (*a*, *b*, *c*, and *V*) except β exhibit a systematic upward trend. This behavior reflects the expected thermal expansion of the crystal lattice, attributed to enhanced atomic vibrations and weakened intermolecular interactions at elevated temperatures. Such expansion is however consistent too with a transition from the LS to the HS state, typically characterized by elongated Fe-N bond lengths and an expanded coordination environment. To intuitively estimate the degree of anisotropy in the unit cell deformation, the relative changes between LS and HS are presented as $\frac{\Delta a}{a} = 1.35\%, \frac{\Delta b}{b} = 4.05\%, \frac{\Delta c}{c} \approx 1.50\%$, respectively. Interestingly, a meticulous examination of the thermal-dependence of the *a* parameter (Fig. 8a) shows that on heating, it first starts to decrease, which is the signature of *a* thermal relaxation. This means that on cooling, the lattice spacing along *a* remained in some metastable state due to its rigidity which is reflected in its lower relative change at the transition. Compared to the behavior of the unit cell parameters, the β angle showed a slight decrease with increasing temperature. This deformation is likely due to structural adjustments linked to the spin state transition, where the lattice adapts to the larger spatial demands of the HS state. The unit cell volume increases by ~ 6.9 % with increasing temperature, highlighting the significant structural changes accompanying the SCO process. This observation is consistent with previous reports on volume expansion during spin state transitions.[55,56]

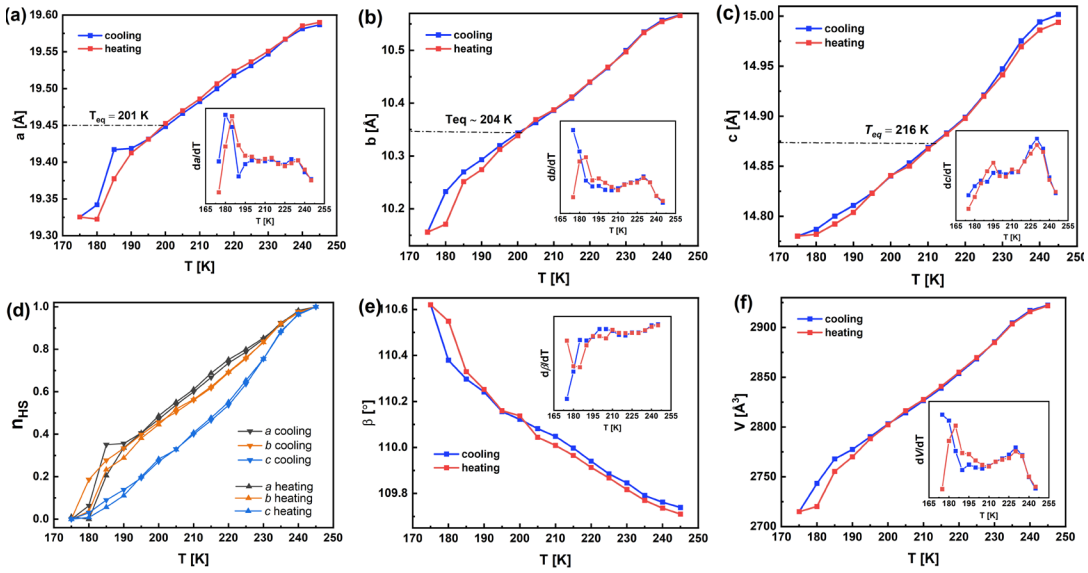

Figure 8. Thermal-dependence of the lattice parameters, *a* (a), *b* (b) and *c* (c) during the cooling and heating processes at static temperatures. Normalized cell parameters at variable temperatures during the cooling and heating processes (d), showing a singular behavior for the lattice parameter, *c*. Angle β *vs. T* during the cooling and heating processes (e). Unit cell volume, *V*, *vs. T* during the cooling and heating processes (f). In insets of panels, (a), (b), (c), (e) and (f), are represented the derivatives with respect to temperature of the plotted quantities, enabling transition temperatures to be identified.

Careful examination of cell parameters temperature evolution reveals that lattice parameters switch from HS to LS in three stages. This feature is well-visible in the behavior of the first derivatives of lattice parameters, d*x*/d*T* (*x* = *a*, *b*, *c*), presented in the insets of Figs. 8a, 8b and 8c. These transitions correspond well to the magnetic, DSC and OM results discussed above. The derivatives of lattice parameters *a* and *b* peak at the following temperatures, T_1 = 185 K, T_2 = 195 K and T_3 = 230 K, while that of *c* exhibit singularities at $T_1^{\uparrow}$ = 195 K, $T_2^{\uparrow}$ = 210 K and $T_3^{\uparrow}$ = 230 K on warming, and on cooling at $T_1^{\downarrow}$ = 185 K, $T_2^{\downarrow}$ = 195 K and $T_3^{\downarrow}$ = 230 K. On the other hand, if we define the average transition temperature T_{eq}, as the value at which the lattice parameter *x* (*x*=*a, b, c*) becomes equal to (x_{HS}+x_{LS})/2, then we find that the lattice parameters *a* and *b* switch at T_{eq} = 201 and 204 K, respectively, while *c* converts at T_{eq} = 216 K (Figure 8c). The average transition temperature of *c* is much higher than that of *a* and *b*, which is remarkable, as clearly shown in panel (d) which summarizes the thermal-dependence of the normalized *a, b, c* lattice parameters. These temperatures are in line with the multi-step character of the transition obtained in magnetism, DSC and OM, which leads to quite close transition temperature values.

Actually, the observed strong anisotropy of lattice parameter changes does not appear as the only parameter from which originates the multi-step character of the transition. Worth to consider are the Fe1–N bond lengths (Table S2), which show differential

changes. Interestingly, not all Fe1-N bonds change in the same amount: Fe1-N5 and Fe1-N6 which are located along the *b* axis both increase for 11% and 12%. Fe1-N4 and Fe1-N7, located along *a*+*c* and *a*-*c* directions, respectively, only increase for approx. 9%.

The previous anisotropic behavior is further corroborated by the unit cell parameters, where the *a* and *c* axes increase by $\frac{\Delta a}{a} = 1.35\%$, $\frac{\Delta c}{c} \approx 1.50\%$ between 175 K and 245 K, while the *b*-axis undergoes a more pronounced expansion of $\frac{\Delta b}{b} = 4.05\%$, which makes the trend of the change in the unit cell volume during the SCO process consistent with that of the *b*-axis (Figure 8b and 8f). Indeed, although the relative change of *b* lattice parameter is rather large, its associated thermal change does not differ from *a* parameter (identical transition temperatures). It is worth mentioning the important difference in the LS region (175-200 K) between the normal thermal expansion coefficient $\alpha_i = \frac{d}{dT} \ln x_i$ ($x_1 = a, x_2 = b, x_3 = c$) along the three directions of the unit cell: $\alpha_a^{LS} = 261 \times 10^{-6}$ K^{-1}, $\alpha_b^{LS} = 901 \times 10^{-6}$ K^{-1} and $\alpha_c^{LS} = 50 \times 10^{-6}$ K^{-1}. This means that in the LS state, the unit cell is more rigid along the *c* and *a* directions compared to the *b* direction, leading the *c* parameter to convert at higher temperatures (Figure 8d).

The next investigation was inspired by reviewer's remarks and comments. Indeed, a meticulous analysis of the lattice deformation shows that the directions along which the Fe octahedron is expanding, when switching from the LS to HS state, are oriented along *b*, (*a*+*c*) and (*a*-*c*) directions. It is therefore interesting to characterize the transition along these directions, by analyzing the relative expansions. The corresponding distances are obtained from the relations $|\vec{a} \pm \vec{c}| = \sqrt{a^2 + c^2 \pm 2\,ac\,\cos\beta}$, which are plotted in Figure S13 *vs.* temperature, using the data of Figure 8. The results are summarized in Table 1 below.

We found that the relative lattice expansions along these directions, between LS and HS phases, are respectively $\frac{\Delta(|\vec{a}+\vec{c}|)}{|\vec{a}+\vec{c}|} = 1.24\%$ and $\frac{\Delta(|\vec{a}-\vec{c}|)}{|\vec{a}-\vec{c}|} = 2.74\%$. First, it appears that the relative deformation along (*a*-*c*) is more than twice of that of (*a*+*c*), while both are significantly weaker than that along the b-direction ($\frac{\Delta b}{b} = 4.05\%$), along which the main crystal deformation is observed in OM experiments.

These highly anisotropic changes are considered to be at the origin of the elastic frustration causing the present multi-step character of the spin transition observed in **1**.

This assignment is in line with existing theoretical developments. The connection between the anisotropic or directional character of elastic interactions and the multistep nature of the spin transition has been addressed theoretically, beginning with the first paper that introduced the concept of elastic frustration in a 2D system[57], and further developed in subsequent works by Cruddas *et al.*[58] and Ndiaye *et al.*[59] More recently, a 3D elastic model was implemented by Belmouri *et al.*,[60] in which the multi-step character of the SCO transition, accompanied by the self-organization of spin states, was evidenced through the relaxation curves of the metastable HS fraction at low temperature. However, to definitely assess the present assignment, this theoretical work must be extended to the study of thermally-induced spin transitions.

Table 1: Relative lattice parameter changes of **1** showing strong anisotropic deformation of the lattice along (*a*+*c*), (*a*-*c*) and *b* directions.

T (K)	100	200	300(1)	300(2)
a (Å)	19.2513(13)	19.4295(9)	19.5743(11)	19.5742(11)
b (Å)	10.1642(4)	10.3396(3)	10.5700(4)	10.5721(4)
$\frac{\Delta b}{b}$	-	1.73%	4.00%	4.02%
c (Å)	14.6855(9)	14.7741(7)	14.9557(9)	14.9619(8)
α (°)	90	90	90	90
β (°)	110.468(5)	110.097(4)	109.633(4)	109.659(4)
γ (°)	90	90	90	90
$\lvert\vec{a}-\vec{c}\rvert$	28.000	28.161	28.347	28.356
$\frac{\Delta\lvert\vec{a}-\vec{c}\rvert}{\lvert\vec{a}-\vec{c}\rvert}$	-	0.575%	1.24%	1.27%
$\lvert\vec{a}+\vec{c}\rvert$	19.712	19.963	20.251	20.247
$\frac{\Delta\lvert\vec{a}+\vec{c}\rvert}{\lvert\vec{a}+\vec{c}\rvert}$	-	1.27%	2.74%	2.72%

From a mechanistic point of view, valuable information can be extracted from the alliance of XRD data and simple considerations related to thermal expansion of the lattice. Using the thermal-dependence of $(a+c)$, $(a-c)$ and b, we could derive the corresponding thermal expansion coefficients, denoted α_x^T [$\alpha_x^T = \frac{d}{dT}(\ln x)$] where x = *a*, *b*, *c*, (*a*-*c*), (*a*+*c*), some of them being depicted in Figure 9.

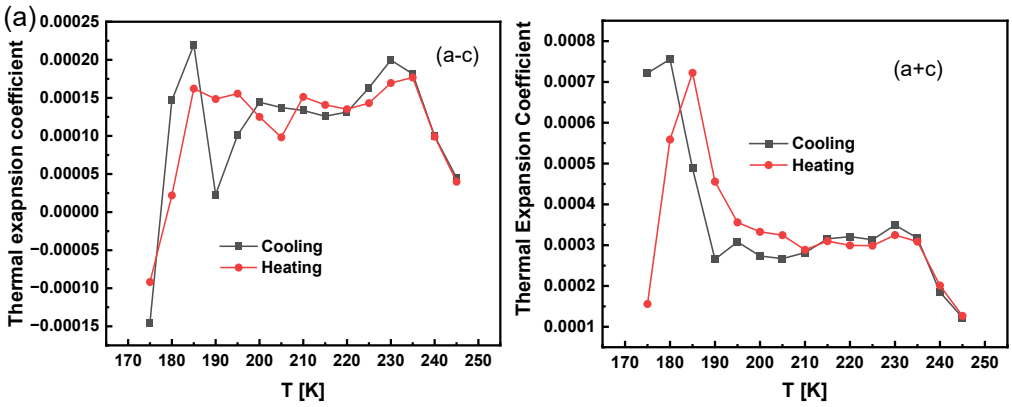

Figure 9: Thermal variation of the thermal expansion coefficient along (*a*-*c*) and (*a*+*c*) extracted from XRD measurements for **1**.

Table S7 summarizes the values of the thermal expansion coefficients, showing that α_x^T along (*a*-*c*) direction in the LS region is ten times smaller than that of (*a*+*c*), which is also nearly two times smaller than that along *b*-direction. This strongly suggests the existence of a significant anisotropy in the thermal flexibility or rigidity of the lattice between these directions.

Quantitative comparison between magnetism, DSC, OM and X-ray data

DSC signals were plotted together with the first derivative of $\chi_M T$ and n_{HS} derived from OM, as well as *c* lattice parameter in the warming mode (Figure 10) to better compare transition temperatures *via* the maximum of the curves. Overall, a good match is found between calorimetric and magnetic data in both high-temperature and low-temperature regions, while OM transition temperatures are slightly shifted to higher temperatures (Table 2). The agreement between magnetic and DSC measurements is not surprising because both experiments represent an average response of the system with a collection of crystals, contrary to OM studies and X-ray which bring the response of one single crystal. Thus, the shift of OM peaks by 4-6 K at low temperature and almost 8-11 K at high temperature region are attributed to the specific character of transition temperatures of each single crystal, which depend on its microstructure, shape, size, defects *etc.*[61-63] The differences observed between OM (Figure 7) and XRD (Figure 8) data mainly arise from the experimental configurations. OM provides high temporal resolution with continuous temperature sweep and fast image acquisition (10 frames/s), allowing precise tracking of the spin transition. In contrast, XRD data were collected at discrete temperatures with long stabilization times (~15 min per point), resulting in lower sampling density and smoothing of transition features. These factors explain the sharper transitions seen in OM compared to XRD.

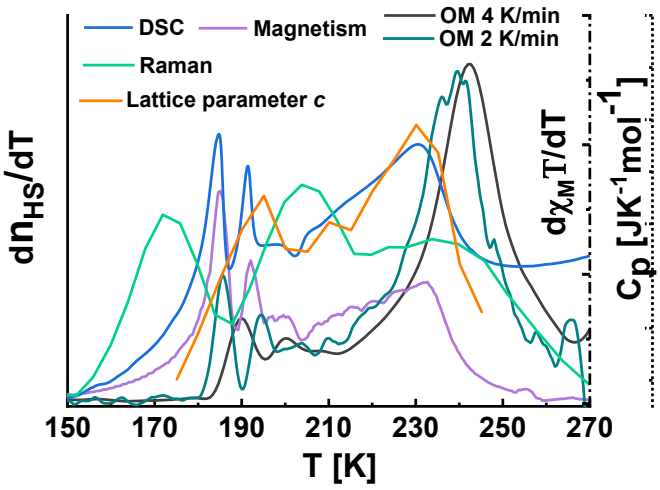

Figure 10. Thermal dependence (along with the heating process) of the DSC response (blue curve, scan rate 5 K min^{-1}), compared with the first derivative of the magnetic (violet curve 2 K min^{-1}**)**, OM signal (black curve, 4 K min^{-1} and green curve, 2 K min^{-1}), Raman (light green) and lattice parameter *c* from X-ray diffraction (orange). An excellent agreement is found between magnetism and DSC studies. OM data are slightly shifted to higher temperatures.

Table 2. Transition temperatures for magnetism, DSC, OM, X-ray and Raman measurements.

Physical method	Cooling			Heating		
	$T_1{\downarrow}$	$T_2{\downarrow}$	$T_3{\downarrow}$	$T_1{\uparrow}$	$T_2{\uparrow}$	$T_3{\uparrow}$
Magnetism (2 K min^{-1})	183 K	192 K	232 K	185 K	192 K	231 K
DSC (5 K min^{-1})	181 K	189 K	229 K	185 K	191 K	230 K
OM (2 K min^{-1})	176 K	184 K	232 K	186 K	194 K	240 K
OM (4 K min^{-1})	173 K	184 K	229 K	190 K	200 K	242 K
X-ray (*c-axis*)	185 K	195 K	230 K	195 K	210 K	230 K
Raman (1 K min^{-1})	173 K	202 K	236 K	174 K	204 K	236 K

Correlating Crystallographic, Optical and Mechanical Transformations

The crystallographic data collected and analyzed in Table S6 were used to compare the length of the single crystal **1**, ~ 231 µm × 107 µm in surface size (Figures 6 and S10). The OM data lead to relative length changes of 4% for **1** along the spin transition (Table S8), in excellent agreement with X-ray data along *b* lattice parameter. These crystals which are resilient during the transition were studied in the low and in the high-temperature process. In Figure 11, the normalized crystal length n_{Length} and the HS fraction, n_{HS}, are both represented. We also introduced the normalized crystallographic parameters. It should be noted that the crystal's edge detection parameters are very

uncertain in determining its length as a function of temperature. This is strongly related to the resolution of the images and the stability of the images due to the vibration of the cryostat with vacuum pumping, which are the main causes of uncertainty in the present work. In this study, we can see that the mechanical transformation takes place before the macroscopic spin transition related to the color change of microscopy images. Figure 11 shows the heating process, where we also have a multi-step transformation of the crystal elongation. This behavior shows once again the importance of elasticity and also that the macroscopic mechanical change precedes the macroscopic spin transition observed by microscopy. This result is predictable, as it has already been visualized on other types of SCO single crystals by optical interference techniques.[64-67] In previous work, Sy and Boukheddaden[68] by using an optical interference method showed that in SCO materials, the propagation of the macroscopic HS/LS interface can be affected by mechanical stresses generated by the volume change during the transition. They observed the thermally induced contraction or expansion of crystals involving volume changes before the phase transition related by the optical density changing macroscopic on the single crystals.

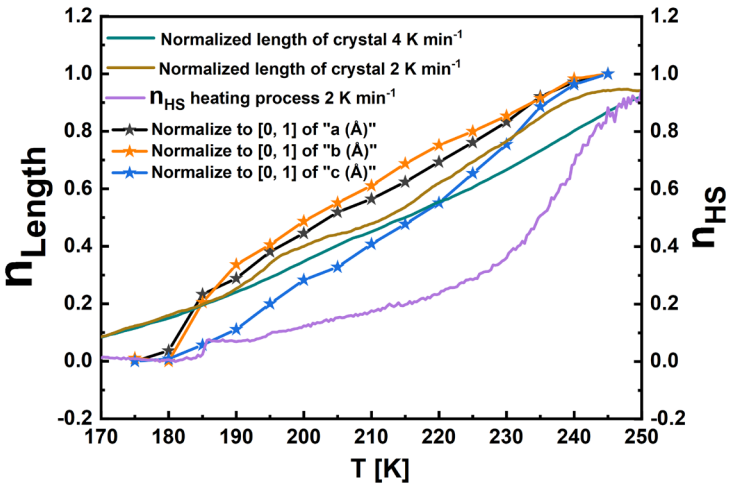

Figure 11. Temperature dependence of normalized length of crystal n_{Length} in heating and cooling modes compared of the high-spin fraction, n_{HS}, at 2 K min^{-1} (magenta curve). Lattice parameters *a*, *b* and *c* during heating process are shown too.

DISCUSSION

To better understand the multistep SCO behavior observed in **1**, we have compared our system with previously reported multistep SCO materials, particularly Hofmann-type coordination frameworks and "Soma–Iwamoto-type" complexes (Table S9). In many gold- or silver-bridged SCO compounds, the occurrence of stepwise transitions is often

attributed to the presence of multiple crystallographically distinct Fe(II) sites or to symmetry-lowering phase transitions, which promote long-range ordering of HS/LS states. For example, {Fe(4-MeOPmd)$_2$[Ag(CN)$_2$]$_2$·0.25(4-MeOPmd)}(1Ag·0.25G), reported by Kitase *et al.*,[43] exhibits a gradual three-step SCO behavior, which arises from its complex interpenetrated bilayer structure comprising five inequivalent Fe^{2+} sites that undergo HS to LS conversion in a temperature-dependent sequential manner. In such compounds, aurophilic interactions are often observed. Although Au···Au interactions do not directly influence the electronic structure associated with SCO, they play an important role in crystal engineering by locking conformations and reinforcing interlayer coupling, thereby facilitating stepwise rather than cooperative transitions.

For **1**, although the Au···Au distances exceed the typical range of strong aurophilic interactions (> 7.0 Å), the associated π–Au and π–π interactions serve a comparable function by enhancing supramolecular coherence and supporting a pseudo-three-dimensional packing favorable for gradual SCO.

Another well-known family of multistep SCO compounds includes Hofmann-type frameworks featuring square-planar $[M^{II}(CN)_4]^{2-}$ units (M = Pd, Pt). These are generally classified into two categories: 2D layered structures based on 1,2,4-triazole derivatives and 3D network structures incorporating pyridyl-based ligands. In these materials, the presence of guest molecules and elastic frustration are the principal factors that induce multistep SCO behavior. For instance, Murphy *et al.* reported a porous 2D Hofmann-type framework $[Fe^{II}(bztrz)_2(Pd^{II}(CN)_4)]\cdot n(guest)$ (bztrz = (*E*)-1-phenyl-N-(1,2,4-triazol-4-yl)methanimine), showing guest-programmable one-, two-, and three-step SCO behaviors. The competition between ferro- and antiferro-elastic interactions, tuned by the nature and loading of dual-site guest molecules (e.g., H_2O, EtOH), modulates lattice frustration and stabilizes fractional spin states.[21] Likewise, Real *et al*. reported a 3D Hofmann-type porous coordination polymer $\{Fe^{II}(3,8phen)[Au(CN)_2]_2\}\cdot xPhNO_2$ (3,8phen = 3,8-phenanthroline, $PhNO_2$ = nitrobenzene). The incorporated $PhNO_2$ guest functions as a molecular spacer between the interpenetrated 3D networks through specific $PhNO_2$-3,8phen interactions, thereby introducing elastic frustration that gives rise to the observed multistep SCO behavior.[69]

In contrast, the 2D Hofmann-type coordination polymer (**1**) exhibits multistep SCO behavior, despite containing only one crystallographically distinct Fe(II) center and retaining its centrosymmetric lattice (space group *C*2/*c*) in the absence of guest molecules. This atypical behavior is attributed to elastic frustration within the layered framework. These instabilities arise from the strong directional anisotropy in lattice strain along crystallographic axes. Notably, among the two crystallographically distinct

Au sites, only Au2 forms Au···π interactions with aromatic ligands, while Au1 remains non-interacting. This functional asymmetry introduces directionally selective supramolecular constraints: Au2 acts as a rigid anchor enhancing interlayer coupling, whereas Au1 provides greater local structural flexibility. Together, these interactions impose anisotropic mechanical restrictions along specific crystallographic directions, leading to spatially resolved Fe-N bond contraction during the SCO process. Variable-temperature lattice parameter analysis (e.g., a more pronounced contraction in the *b*-axis and a delayed contraction in the *c*-axis)) confirms direction-dependent rigidity and stepwise structural response. Although the global crystal symmetry remains unchanged, the inhomogeneous internal strain distribution allows for local phase separation without a crystallographic phase transition. This mechanism differs fundamentally from the symmetry-breaking transitions commonly observed in other multistep SCO systems and highlights the unique structure–function interplay of this material.

CONCLUSION

The first two-dimensional Hofmann-like complex using a 1,2,4-triazole derivative as ligand and bridged by $[Au(CN)_2]^-$ units was synthesized in the search of new multistep spin transitions. A set of relevant physical characterization techniques, including thermally induced magnetic susceptibility, differential scanning calorimetry, single crystals X-ray diffraction, Raman spectroscopy and optical microscopy, were used to analyze its three-step spin crossover behavior. The presence of various supramolecular interactions, including hydrogen bonding, Au···π, and π···π stacking contacts, as demonstrated by X-ray diffraction studies, contributes to the anisotropic rigidity of the unit cell along the three lattice parameters. This pronounced anisotropy is considered to underline the elastic frustration responsible for the multistep nature of the transition, in line with recent theoretical models addressing such behavior. This work completes the study of Hofman-type spin crossover compounds and opens the possibility to generate multistep spin transition by introducing anisotropic supramolecular interactions.

ASSOCIATED CONTENT

SI Supporting Information

The Supporting Information is available free of charge at xxx

General information, syntheses, crystal data, IR, PXRD, SEM, optical properties and movies.

Accession Codes

Deposition numbers 2389993−2389996 contain the supplementary crystallographic data for this paper. These data can be obtained free of charge via www.ccdc.cam.ac.uk/data_request/cif, or by emailing data_request@ccdc.cam.ac.uk, or by contacting The Cambridge Crystallographic Data Centre, 12 Union Road, Cambridge CB2 1EZ, U.K.; fax: +44 1223 336033.

AUTHOR INFORMATION

Corresponding Authors

Yann Garcia - *Institute of Condensed Matter and Nanosciences, Molecular Chemistry, Materials and Catalysis (IMCN/MOST), Université catholique de Louvain, 1348 Louvain-la-Neuve, Belgium*

https://orcid.org/0000-0002-3105-0735

E-mail: yann.garcia@uclouvain.be

Kamel Boukheddaden - *Université Paris-Saclay, UVSQ, CNRS, GEMAC UMR 8635, 45 Avenue des Etats Unis, F78035 Versailles Cedex, France*

https://orcid.org/0000-0003-0464-1609

E-mail: kamel.boukheddaden@uvsq.fr

Authors

Xiaochun Li - *Institute of Condensed Matter and Nanosciences, Molecular Chemistry, Materials and Catalysis (IMCN/MOST), Université catholique de Louvain, 1348 Louvain-la-Neuve, Belgium*

Nour El Islam Belmouri - *Université Paris-Saclay, UVSQ, CNRS, GEMAC UMR 8635, 45 Avenue des Etats Unis, F78035 Versailles Cedex, France*

Mouhamadou Sy - *Université Paris-Saclay, UVSQ, CNRS, GEMAC UMR 8635, 45 Avenue des Etats Unis, F78035 Versailles Cedex, France; Université Assane Seck de Ziguinchor, Département de Physique, LCPM, BP 523 Diabir, Ziguinchor 27000, Sénégal*

Mariusz Wolff - *Institute of Functional Materials and Catalysis, Faculty of Chemistry, University of Vienna, Währinger Str. 38-42, 1090 Vienna, Austria*

Aurelian Rotaru - *Department of Electrical Engineering and Computer Science and MANSiD Research Center, "Stefan cel Mare" University, University Street, 13,*

Suceava 720229, Romania

Steven van Terwingen - *Institute of Inorganic Chemistry, Faculty of Chemistry, University of Vienna, Währinger Str. 42, 1090 Vienna, Austria*

Dominik Maskowicz - *Photophysics Department, The Szewalski Institute of Fluid-Flow Machinery, Polish Academy of Sciences, Fiszera 14, 80-231 Gdańsk, Poland*

Miroslaw Sawczak - *Photophysics Department, The Szewalski Institute of Fluid-Flow Machinery, Polish Academy of Sciences, Fiszera 14, 80-231 Gdańsk, Poland*

Rafal Jendrzejewski - *Photophysics Department, The Szewalski Institute of Fluid-Flow Machinery, Polish Academy of Sciences, Fiszera 14, 80-231 Gdańsk, Poland*

Notes

The authors declare no competing financial interest.

ACKNOWLEDGMENTS

This work was supported through the Fonds De La Recherche Scientifique—FNRS (PDR T.0095.21, CDR J.0064.23, EQP U.N027.24 and PINT-BILAT-M PAS Poland), the Université de Versailles-Paris Saclay, CNRS and Mol-CoSM ANR Project N° ANR-20-CE07-0028-01 and UEFSCDI through the project number PNIII-P1-1.1-TE-2019-2194 (Contract No: TE 123/2020). X. L. was supported by fellowship from the China Scholarship Council (202108310050) and a Bourse de voyage FWB to visit Paris Saclay. The authors gratefully acknowledge the Mass Spectrometry Center and the Core Facility for Crystal Structure Analysis, Faculty of Chemistry, University of Vienna.

REFERENCES

1. Zhou, P.; Fu, Y.; Wang, M.; Qiu, R.; Wang, Y.; Stoddart, J. F.; Wang, Y.; Chen, H. Robust Single-Supermolecule Switches Operating in Response to Two Different Noncovalent Interactions. *J. Am. Chem. Soc.* **2023**, *145*, 18800-18811.

2. Ling, B.-K.; Chang, M.; Zhai, Y.-Q.; Deng, J.; Kofu, M.; Guo, H.; Zhao, J.; Fu, Z.; Zheng, Y.-Z. Quantum Spin Wave Excited from a Cr–Dy Single-Molecule Magnet. *J. Am. Chem. Soc* **2025**, 147, 10935-10942.

3. Garcia, Y.; Robert, F.; Naik, A. D.; Zhou, G.; Tinant, B.; Robeyns, K.; Michotte, S.; Piraux, L. Spin Transition Charted in a Fluorophore-Tagged Thermochromic Dinuclear Iron(II) Complex. *J. Am. Chem. Soc.* **2011**, *133*, 15850-15853.

4. Gütlich, P.; Gaspar, A. B., Garcia, Y. Spin State Switching in Iron Coordination Compounds. *Beilstein J. Org. Chem.*, **2013**, *9*, 342-391.

5. Sun, L; Li, X.; Vandenbulcke, C.; Belmouri, N. El I.; Bouchez, G.; Robeyns, K.; Rotaru, A.;

Boukheddaden, K.; Garcia, Y. Stimuli-Responsive Spin Crossover Behavior in 3D Fe(II) Porous Coordination Polymers for Guest Molecules. *Mater. Adv*. **2024**, 5, 8564-8574.

6. Kumar, V; Rotaru A.; Garcia, Y. Room Temperature Light Induced Spin State Switching in a Fe^{II} Coordination Polymer Featuring a Photo Responsive Anion. *J. Mater. Chem. C.* **2022**, *10*, 14128-14134.

7. Clements, J. E.; Price, J. R.; Neville, S. M.; Kepert, C. J. Hysteretic Four-Step Spin Crossover within a Three-Dimensional Porous Hofmann-like Material. *Angew. Chem. Int. Ed.* **2016**, *128*, 15329-15333.

8. Sciortino, N. F.; Ragon, F.; Zenere, K. A.; Southon, P. D.; Halder, G. J.; Chapman, K. W.; Piñeiro-López, L.; Real, J. A.; Kepert, C. J.; Neville, S. M. Exploiting Pressure to Induce a "Guest-Blocked" Spin Transition in a Framework Material. *Inorg. Chem*. **2016**, *55*, 10490.

9. Nakano, K.; Kawata, S.; Yoneda, K.; Fuyuhiro, A.; Yagi, T.; Nasu, S.; Morimoto, S.; Kaizaki, S. Direct Two-Step Spin-Crossover through [HS–HS]···[LS–LS] at the Plateau in Dinuclear Diiron(ii) Complex $[\{Fe(NCBH_3)(4phpy)\}_2(\mu\text{-bpypz})_2]$. *Chem. Commun.* **2004**, 2892-3.

10. Zheng, C.; Jia, S.; Dong, Y.; Xu, J.; Sui, H.; Wang, F.; Li, D. Symmetry Breaking and Two-Step Spin-Crossover Behavior in Two Cyano-Bridged Mixed-Valence $\{Fe^{III}_2(\mu\text{-}CN)_4Fe^{II}_2\}$ Clusters. *Inorg. Chem*. **2019**, *58*, 14316-14324.

11. Garcia, Y.; Kahn, O.; Rabardel, L.; Chansou, B.; Salmon, L.; Tuchagues, J. P. Two-Step Spin Conversion for the Three-Dimensional Compound Tris(4,4'-bis-1,2,4-triazole)iron(II) Diperchlorate. *Inorg. Chem*. **1999**, *38*, 4663-4670.

12. Sciortino, N. F.; Scherl-Gruenwald, K. R.; Chastanet, G.; Halder, G. J.; Chapman, K. W.; Létard, J.-F.; Kepert, C.J. Hysteretic Three-Step Spin Crossover in a Thermo- and Photochromic 3D Pillared Hofmann-type Metal-Organic Framework. *Angew. Chem. Int. Ed.* **2012**, *51*, 10154-10158.

13. Munoz, M. C.; Gaspar, A. B.; Galet, A.; Real, J. A. Spin-Crossover Behavior in Cyanide-Bridged Iron(II)−Silver(I) Bimetallic 2D Hofmann-like Metal−Organic Frameworks. *Inorg. Chem*. **2007**, *46*, 8182-8192.

14. Klingele, M. H.; Moubaraki, B.; Cashion, J. D.; Murray, K. S.; Brooker, S. The First X-ray Crystal Structure Determination of a Dinuclear Complex Trapped in the [Low Spin–High Spin] State: $[Fe^{II}_2(PMAT)_2](BF_4)_4\cdot$DMF. *Chem. Commun* **2005**, 987-989.

15. Neville, S. M.; Leita, B. A.; Halder, G. J.; Kepert, C. J.; Moubaraki, B.; Létard, J. F.; Murray, K. S. Understanding the Two-Step Spin-Transition Phenomenon in Iron(II) 1D Chain Materials. *Chem. Eur. J.* **2008**, *14*, 10123-10133.

16. Sciortino, N. G.; Zenere, K. A.; Corrigan M. E.; Halder, G. J.; Chastanet, G.; Létard, J. -F.; Kepert, C. J.; Neville S. M. Four-Step Iron(II) Spin State Cascade Driven by Antagonistic Solid State Interactions. *Chem. Sci.* **2017**, *8*, 701-707.

17. Wu, Y. Y.; Xu, G. Y.; Yan, Z. H.; Zhou, X. Y.; Yang, F. L.; Dai, J. W.; Wu, Dai S. Q.; Li, Z. Y.; Sato, O. Altered Mode of Structural Changes in Solid Solutions Leading to Dual Modulation: Spin Transition Temperatures and Steps. *J. Am. Chem. Soc*. **2025**, *147*, 14401-14410.

18. Peng, Y.-Y.; Wu, S.-G.; Chen, Y.-C.; Liu, W.; Huang, G.-Z.; Ni, Z.-P.; Tong, M.-L. Asymmetric

Seven-/Eight-Step Spin-Crossover in a Three-Dimensional Hofmann-Type Metal–Organic Framework. *Inorg. Chem. Front.* **2020**, *7*, 1685-1690.

19. Klein, Y. M.; Sciortino, N. F.; Ragon, F.; Housecroft, C. E.; Kepert, C. J.; Neville, S. M. Spin Crossover Intermediate Plateau Stabilization in a Flexible 2-D Hofmann-Type Coordination Polymer. *Chem. Commun.* **2014**, *50*, 3838-3840.

20. Ohtani, R.; Yoneda, K.; Furukawa, S.; Horike, N.; Kitagawa, S.; Gaspar, A. B.; Munoz, M. C.; Real, J. A.; Ohba, M. Precise Control and Consecutive Modulation of Spin Transition Temperature Using Chemical Migration in Porous Coordination Polymers. *J. Am. Chem. Soc.* **2011**, *133*, 8600-8605.

21. Murphy, M. J.; Zenere, K. A.; Ragon, F.; Southon, P. D.; Kepert, C. J.; Neville, S. M. Guest Programmable Multistep Spin Crossover in a Porous 2-D Hofmann-Type Material. *J. Am. Chem. Soc.* **2017**, *139*, 1330-1335.

22. Ahmed, M.; Brand, H. E.; Peterson, V. K.; Clegg, J. K.; Kepert, C. J.; Price, J. R.; Powell, B. J.; Neville, S. M. Dual-Supramolecular Contacts Induce Extreme Hofmann Framework Distortion and Multi-Stepped Spin-Crossover. *Dalton Trans.* **2021**, *50*, 1434-1442.

23. Brennan, A. T.; Zenere, K. A.; Brand, H. E.; Price, J. R.; Bhadbhade, M. M.; Turner, G. F.; Moggach, S. A.; Valverde-Munoz, F. J.; Real, J. A.; Clegg, J. K. Guest Removal and External Pressure Variation Induce Spin Crossover in Halogen-Functionalized 2-D Hofmann Frameworks. *Inorg. Chem.* **2020**, *59*, 14296-14305.

24. Zenere, K. A.; Duyker, S. G.; Trzop, E.; Collet, E.; Chan, B.; Doheny, P. W.; Kepert, C. J.; Neville, S. M. Increasing Spin Crossover Cooperativity in 2D Hofmann-Type Materials with Guest Molecule Removal. *Chem. Sci*. **2018**, *9*, 5623-5629.

25. Milin, E.; Patinec, V.; Triki, S.; Bendeif, E.-E.; Pillet, S.; Marchivie, M.; Chastanet, G.; Boukheddaden, K. Elastic Frustration Triggering Photoinduced Hidden Hysteresis and Multistability in a Two-Dimensional Photoswitchable Hofmann-Like Spin-Crossover Metal–Organic Framework. *Inorg. Chem.* **2016**, *55*, 11652-11661.

26. Brennan, A. T.; Zenere, K. A.; Kepert, C. J.; Clegg, J. K.; Neville, S. M. Three Distinct Spin-Crossover Pathways in Halogen-Appended 2D Hofmann Frameworks. *Inorg. Chem.* **2021**, *60*, 3871-3878.

27. Ahmed, M.; Zenere, K. A.; Sciortino, N. F.; Arachchige, K. S.; Turner, G. F.; Cruddas, J.; Hua, C.; Price, J. R.; Clegg, J. K.; Valverde-Muñoz, F. J. Regulation of Multistep Spin Crossover Across Multiple Stimuli in a 2-D Framework Material. *Inorg. Chem.* **2022**, *61*, 6641-6649.

28. Shylin, S. I.; Kucheriv, O. I.; Shova, S.; Ksenofontov, V.; Tremel, W.; Gural'skiy, I. y. A. Hofmann-Like Frameworks Fe(2-methylpyrazine)n[$M(CN)_2]_2$ (M = Au, Ag): Spin-Crossover Defined by the Precious Metal. *Inorg. Chem.* **2020**, *59*, 6541-6549.

29. Yoshida, K.; Akahoshi, D.; Kawasaki, T.; Saito, T.; Kitazawa, T. Guest-Dependent Spin Crossover in a Hofmann-Type Coordination Polymer Fe(4,4'-bipyridyl)[$Au(CN)_2]_2 \cdot n$Guest. *Polyhedron* **2013**, *66*, 252-256.

30. Kosone, T.; Tomori, I.; Kanadani, C.; Saito, T.; Mochida, T.; Kitazawa, T. Unprecedented

Three-Step Spin-Crossover Transition in New 2-Dimensional Coordination Polymer {Fe^{II}(4-methylpyridine)$_2$[Au^{I}(CN)$_2$]$_2$}. *Dalton Trans.* **2010**, *39*, 1719-1721.

31. Kitase, K.; Akahoshi, D.; Kitazawa, T. Effects of Both Methyl and Pyrimidine Groups in Fe–Ag Spin-Crossover Hofmann-Type Complex {Fe(4-Methylpyrimidine)$_2$[Ag(CN)$_2$]$_2$}. *Inorg. Chem.* **2021**, *60*, 4717-4722.

32. Li, J. Y.; Chen, Y. C.; Zhang, Z. M.; Liu, W.; Ni, Z. P.; Tong, M. L. Tuning the Spin-Crossover Behaviour of a Hydrogen-Accepting Porous Coordination Polymer by Hydrogen-Donating Guests. *Chem. Eur. J.* **2015**, *21*, 1645-1651.

33. Kosuge, R.; Kawasaki, T.; Kitase, K.; Kosone, T. The Synthesis and Crystal Structures of New One- and Two-Dimensional Fe(II) Coordination Polymers Using Imidazole Derivatives. *Crystals* **2023**, *13*, 1658.

34. Kitase, K.; Akahoshi, D.; Kitazawa, T. Soma–Iwamoto-Type SCO Complex Fe(quinazoline)$_2$[Au(CN)$_2$]$_2$ Using the Quinazoline-Type Ligand. *Dalton Trans.* **2024**, *53*, 9248-9251.

35. Ezzedinloo, L.; Zenere, K. A.;Xie, Z.; Ahmed, M.; Scottwell, S.; Bhadbhade, M.; Brand, H. E. A.; Clegg, J. K.; Hua, C.; Sciortino, N. F.; Parker, L. C.; Powell, B. J.; Kepert, C. J.; Neville, S. M. Hierarchical Spin-Crossover Cooperativity in Hybrid 1D Chains of Fe^{II}-1,2,4-Triazole Trimers Linked by $[Au(CN)^2]^-$ Bridges. *Chem. Eur. J.* **2021**, *27*, 5136-5141.

36. Hiiuk, V. M.; Shylin, S. I.; Barakhtii, D. D.; Korytko, D. M.; Kotsyubynsky, V. O.; Rotaru, A.; Shova, S.; Gural'skiy, I. A. Two-Step Spin Crossover in Hofmann-Type Coordination Polymers [Fe(2-phenylpyrazine)$_2${M(CN)$_2$}$_2$] (M = Ag, Au). *Inorg. Chem.* **2022**, *61*, 2093-2104.

37. Remili, Y.; Nasimsobhan, M.; Turo-Cortes, R.; Vendier, L.; Bartual-Murgui, C.; Molnar, G.; Bousseksou, A.; Real, J. A., Raman scattering and X-ray diffraction study of the temperature- and pressure-induced multistep spin transition in the complex {Fe^{II}(AnPy)$_2$[Ag^{I}(CN)$_2$]$_2$}·NO_2bz. *Phys. Chem. Chem. Phys.* **2025**, *27*, 21593-21603.

38. Kosone, T.; Makido, Y.; Okuda, S.; Haigo, A.; Kawasaki, T.; Akahoshi, D.; Saito, T.; Kitazawa, T. Systematic Design of Crystal Structure for Hofmann-Like Spin Crossover Fe(L)$_2$[Ag(CN)$_2$]$_2$ Complexes. *Crystals* **2019**, *9*, 370.

39. Arcís-Castillo, Z.; Munoz, M. C.; Molnár, G.; Bousseksou, A.; Real, J. A. [Fe(TPT)$_{2/3}${M^{I}(CN)$_2$}$_2$]·*n*Solv (M^{I}=Ag, Au): New Bimetallic Porous Coordination Polymers with Spin-Crossover Properties. *Chem. Eur. J.* **2013**, *19*, 6851-6861.

40. Shoutaro, U.; Takeshi, K.; Jun, O.; Takafumi, K. Structural, Electronic, and Magnetic Properties of Novel Spin-Crossover Complex: Fe(butyl nicotinate)$_2$[Au(CN)$_2$]$_2$. *Bull. Chem. Soc. Jpn.* **2015**, *88*, 551-553.

41. Kitase, K.; Akahoshi, D.; Kitazawa, T. Guest-Triggered “Soma–Iwamoto-Type” Penetration Complex {Fe(4-methoxypyrimidine)$_2$[M(CN)$_2$]$_2$}·Guest (M = Ag, Au). *Dalton Trans.* **2023**, *52*, 2571-2579.

42. Rodríguez-Velamazán, J. A.; Carbonera, C.; Castro, M.; Palacios, E.; Kitazawa, T.; Létard, J. F.; Burriel, R. Two-Step Thermal Spin Transition and LIESST Relaxation of the Polymeric Spin-

Crossover Compounds $Fe(X\text{-}py)_2[Ag(CN)_2]_2$ (X = H, 3-methyl, 4-methyl, 3,4-dimethyl, 3-Cl). *Chem. Eur. J.* **2010**, *16*, 8785-8796.

43. Lada, Z. G. The Investigation of Spin-Crossover Systems by Raman Spectroscopy: A Review. *Magnetochemistry* **2022**, *8*.

44. Lalioti, N.; Charitos, A.; Parthenios, J.; Malina, O.; Polaskova, M.; Petr, M.; Tangoulis, V. Observation of Two-Step Spin Transition in Graphene Oxide-Based Hybrids with Iron(II) 4-amino-1,2,4-triazole Spin Crossover Nanoparticles. *Molecules* **2023**, *28*.

45. Assefa, Z.; Haire, R. G.; Sykora, R. E. Hydrothermal Syntheses, Structural, Raman, and Luminescence Studies of $Cm[M(CN)_2]_3{\cdot}3H2O$ and $Pr[M(CN)_2]_3{\cdot}3H_2O$ (M=Ag, Au): 2. Hetero-Bimetallic Coordination Polymers Consisting of Trans-Plutonium and Transition Metal Elements. *J. Solid State Chem*. **2008**, *181*, 382-391.

46. Gütlich, P.; Garcia, Y.; Goodwin, H. A. Spin Crossover Phenomena in Fe(II) Complexes. *Chem. Soc. Rev.* **2000**, *29*, 419-427.

47. Boukheddaden, K.; Sy, M. Direct Optical Microscopy Observation of Photo-Induced Effects and Thermal Relaxation in a Spin Crossover Single Crystal. *Curr. Inorg. Chem.* **2016**, *6*, 40-48

48. Chong, C.; Slimani, A.; Varret, F.; Boukheddaden, K.; Collet, E.; Ameline, J.-C.; Bronisz, R., Hauser, A. The Kinetics Features of a Thermal Spin Transition Characterized by Optical Microscopy on the Example of $[Fe(bbtr)_3](ClO_4)_2$ Single Crystals: Size Effect and Mechanical Instability. *Chem. Phys. Lett.* **2011**, *504*, 29-33.

49. Slimani, A.; Varret, F.; Boukheddaden, K.; Chong, C.; Mishra; H.; Haasnoot, J. G.; Pillet, S. Visualization and Quantitative Analysis of Spatiotemporal Behavior in a First-Order Thermal Spin Transition: A Stress-Driven Multiscale Process. *Phys. Rev. B*. **2011**, *84*, 094442.

50. Boukheddaden, K; Chong, C.; Mishra, H.; Collet, E.; Haasnoot, J. G.; Pillet, S. The Propagation of the Thermal Spin Transition of $[Fe(btr)_2(NCS)_2]{\cdot}H_2O$ Single Crystals, Observed by Optical Microscopy. *New. J. Chem*. **2011**, *35*, 2333-2340.

51. Chong, C.; Mishra, H.; Boukheddaden, K.; Denise, S.; Bouchez, G.; Collet, E.; Ameline, J. C.; Naik, A. D.; Garcia, Y.; Varret, F. Electronic and Structural Aspects of Spin Transitions Observed by Optical Microscopy. The Case of $[Fe(ptz)_6](BF_4)_2$. *J. Phys. Chem. B.* **2010**, *114*, 1975–1984.

52. Sy, M.; Traiche, R.; Fourati, H.; Singh, Y.; Varret, F.; Boukheddaden, K. Spatiotemporal Investigations on Light-Driven High-Spin–Low-Spin Interface Dynamics in the Thermal Hysteresis Region of a Spin-Crossover Single Crystal. *J. Phys. Chem. C* **2018**, *122*, 20952–20962.

53. Traiche, R.; Sy, M.; Oubouchou, H.; Bouchez, G.; Varret, F.; Boukheddaden, K. Spatiotemporal Observation and Modeling of Remarkable Temperature Scan Rate Effects on the Thermal Hysteresis in a Spin-Crossover Single Crystal. *J. Phys. Chem. C* **2017**, *121*, 11700-11708.

54. Sy, M.; Varret, F.; Boukheddaden, K.; Bouchez, G.; Marrot, J.; Kawata, S.; Kaizaki, S. Structure-Driven Orientation of the High-Spin–Low-Spin Interface in a Spin-Crossover Single Crystal. *Angew. Chem. Int. Ed* **2014**, *53*, 7539-7542.

55. Affes, K.; Slimani, A. ; Maalej, A.; Boukheddaden, K. Electro-elastic modeling of thermal and mechanical properties of spin crossover core/shell nanoparticle. *Chem. Phys. Lett*. **2019**, *718*, 46-

53.
56. Ahmed, M.; Arachchige, K. S. A.; Xie, Z.; Price, J. R.; Cruddas, J.; Clegg, J. K.; Powell, B. J.; Kepert, C. J.; Neville, S. M. Guest-Induced Multistep to Single-Step Spin-Crossover Switching in a 2-D Hofmann-Like Framework with an Amide-Appended Ligand. *Inorg. Chem*. **2022**, *61*, 11667-11674.
57. Zhang, C. J.; Lian, K. T.; Wu, S. G.; Liu, Y.; Huang, G. Z.; Ni, Z. P.; Tong, M.-L. The Substituent Guest Effect on Four-Step Spin-Crossover Behavior. *Chem. Front.* **2020**, *7*, 911-917.
58. Paez-Espejo, M.; Sy, M.; Boukheddaden, K., Elastic Frustration Causing Two-Step and Multistep Transitions in Spin-Crossover Solids: Emergence of Complex Antiferroelastic Structures. *J. Am. Chem. Soc*. **2016**, 138, 3202-10.
59. Cruddas, J.; Powell, B. J., Structure–property relationships and the mechanisms of multistep transitions in spin crossover materials and frameworks. *Inorg. Chem. Front.* **2020,** *7*, 4424-4437.
60. Ndiaye, M.; Boukheddaden, K., Electro-elastic modelling of the two-step high-spin to low-spin relaxation with transient self-organized spin states in 2D spin crossover solids. *J. Phys. Soc. Jpn*. **2020,** *89*, 014004.
61. Belmouri, N.E.I.; di Scala, N; Boukheddaden, K. 3D self-organization of spin crossover multi-layers emerging from the alliance of elastic anisotropy and lattice frustration. *J. Phys. Chem. Solids*. **2024**, *190*, 111985.
62. Boukheddaden, K.; Sy, M.; Varret, F. Emergence of Dynamical Dissipative Structures in a Bistable Spin Crossover Solid Under Light: Experience and Theory. *Advanced Theory and Simulations* **2018**, *1*, 1800080-1800086.
63. Fourati, H.; Ndiaye, M.; Sy, M.; Triki, S.; Chastanet, G.; Pillet, S.; Boukheddaden, K. Light-Induced Thermal Hysteresis and High-Spin Low-Spin Domain Formation Evidenced by Optical Microscopy in a Spin-Crossover Single Crystal. *Phys. Rev. B* **2022**, *105*, 174436-174452.
64. Sy, M., Optical Microscopy Studies of Thermo- and Photo-Induced Spatiotemporal Behaviors and Self-Organization in Switchable Spin Crossover Single Crystal*, Université Paris-Saclay*, **2016**.
65. Fourati, H., Optical Microscopy Studies of Long-Range Behaviours and Thermo- and Photo-Induced Spatiotemporal Effects in Spin Crossover Single Crystals, *Université Paris-Saclay Université de Sfax (Tunisie)*, **2021**.
66. Fourati, H.; Milin, E.; Slimani, A.; Chastanet, G.; Abid, Y.; Triki, S.; Boukheddaden, K. Interplay between a Crystal's Shape and Spatiotemporal Dynamics in a Spin Transition Material. *Phys. Chem. Chem. Phys.* **2018**, *20*, 10142-10154.
67. Paez-Espejo, M.; Sy, M.; Boukheddaden, K. Unprecedented Bistability in Spin-Crossover Solids Based on the Retroaction of the High Spin Low-Spin Interface with the Crystal Bending. *J. Am. Chem. Soc*. **2018**, *140*, 11954-11964.
68. Paez-Espejo, M. Á, Modeling and Simulation of Spatio-Temporal Behaviors of Phase Transitions in Spin Crossover Single Crystals, *Université Paris-Saclay préparée à l'Université Versailles Saint-Quentin en Yvelines*, **2016**.
69. Sy, M.; Boukheddaden, K. Dance of Interference Patterns during the Spin Transition of a Single

Crystal. *J. Phys. Chem. C* **2020**, *124*, 28093-28107.

70. Piñeiro-López, L.; Valverde-Muñoz, F.J.; Trzop, E.; Muñoz, M.C.; Seredyuk, M.; Castells-Gil, J.; da Silva, I.; Martí-Gastaldo, C.; Collet, E.; Real, J.A., Guest induced reversible on–off switching of elastic frustration in a 3D spin crossover coordination polymer with room temperature hysteretic behaviour. *Chem. Sci*. **2021**, *12*, 1317-1326

Table of Contents